

Magnesium radicals MgC_5N and MgC_6H in IRC +10216 [★]

J. R. Pardo¹, C. Cabezas¹, J. P. Fonfría¹, M. Agúndez¹, B. Tercero², P. de Vicente², M. Guélin³, and J. Cernicharo¹

¹ Instituto de Física Fundamental, Consejo Superior de Investigaciones Científicas, C/ Serrano 123, 28006 Madrid, Spain
e-mail: jr.pardo@csic.es, jose.cernicharo@csic.es

² Institut de Radioastronomie Millimétrique, 300 rue de la Piscine, 38406 St-Martin d'Hères, France

³ Instituto Geográfico Nacional, Centro de Desarrollos Tecnológicos, Observatorio de Yebes, Apartado 148, 19080 Yebes, Spain

Received June 29, 2021; accepted July 30, 2021

ABSTRACT

After the previous discovery of MgC_3N and MgC_4H in IRC +10216, a deeper Q-band (31.0-50.3 GHz) integration on this source had revealed two additional series of harmonically related doublets that we assigned on the basis of quantum mechanical calculations to the larger radicals MgC_5N and MgC_6H . The results presented here extend and confirm previous results on magnesium-bearing molecules in IRC +10216. We derived column densities of $(4.7 \pm 1.3) \times 10^{12}$ for MgC_5N and $(2.0 \pm 0.9) \times 10^{13}$ for MgC_6H , which imply that $\text{MgC}_5\text{N}/\text{MgC}_3\text{N} = 0.5$ and $\text{MgC}_6\text{H}/\text{MgC}_4\text{H} = 0.9$. Therefore, MgC_5N and MgC_6H are present with column densities not so different from those of the immediately shorter analogs. The synthesis of these large magnesium cyanides and acetylides in IRC +10216 can be explained for their shorter counterparts by a two-step process initiated by the radiative association of Mg^+ with large cyanopolynes and polyynes, which are still quite abundant in this source, followed by the dissociative recombination of the ionic complexes.

Key words. molecular data — line: identification — stars: carbon — circumstellar matter — stars: individual (IRC +10216) — astrochemistry

1. Introduction

The vast majority of gas-phase metal-bearing molecules detected in space have been observed for the first time in the carbon-rich circumstellar envelope (CSE) IRC +10216. It is worth noting that atomic metals such as Na, K, Ca, Fe, Cr, and/or their cations are found in the gas phase in IRC +10216 (Mauron & Huggins 2010), pointing toward a rich metal chemistry in the outer CSE. The metal halides NaCl, AlCl, KCl, and AlF were the first molecules to contain metals detected in this source and in space (Cernicharo & Guélin 1987). Since these early detections, several new metal-bearing species such as MgNC, MgCN, HMgNC, MgC_3N , MgCCH, MgC_4H , NaCN, SiCN, SiNC, AlNC, KCN, FeCN, and CaNC have been detected (Guélin et al. 1993, 2000, 2004; Kawaguchi et al. 1993; Turner et al. 1994; Ziurys et al. 1995, 2002; Pulliam et al. 2010; Zack et al. 2011; Cabezas et al. 2013; Agúndez et al. 2014; Cernicharo et al. 2019a,b). Among them, the family of metal cyanide and isocyanide species is clearly the most numerous.

Most of the discoveries of these metal-bearing species in IRC +10216 have been done through the interplay between laboratory rotational spectroscopy experiments and radioastronomical observations. Nevertheless, the detection of further metal-containing molecules is hampered by the lack of new spectroscopic data. These molecules are transient species under terrestrial physical conditions and their generation in laboratories is not trivial. In addition, their spectroscopic characterization can be a difficult task because they usually have many electronic states of different multiplicities with similar energies.

The improvements in sensitivity, spectral resolution, and bandwidth achieved by telescopes and receivers in recent years allows one to perform very deep integrations that are powerful spectroscopic tools for analyzing the chemical composition of astronomical objects. Once the lines coming from the isotopologues and vibrationally excited states of already known molecules are identified, a forest of unidentified lines emerges waiting to be assigned such as those registered in a laboratory spectrum. The analysis of these spectral features, supported by high level ab initio calculations, allows one to discover new molecules despite no laboratory data being available. This procedure has recently been employed in the astronomical discovery of MgC_3N and MgC_4H in IRC +10216 (Cernicharo et al. 2019b), and of vibrationally excited HC_7N and HC_9N (Pardo et al. 2020) in this same source. The new sensitive broad band receivers used in this work have also allowed us to detect a large number of molecules in TMC-1, including pure hydrocarbon cycles such as indene and cyclopentadiene (Cernicharo et al. 2021).

In this letter we present the discovery in space of MgC_5N and MgC_6H , from very long Q-band (31.0-50.3 GHz) integrations toward IRC +10216 carried out with the Yebes 40m telescope, and precise quantum chemical calculations. The observational setup is briefly summarized in section 2. The bulk of this letter is section 3, which is devoted to presenting what have been, up to now, two ladders of U-lines from our observations, and their careful analysis aimed at identifying their molecular carriers and ruling out other possible candidates. Although all of the doublets now assigned to MgC_5N ($N = 28-27$ to $N = 41-40$) are well detected and the central frequencies of their separate components can be well established, the same is not so easy for MgC_6H , even if it could be more abundant, due to a much lower dipole moment. Finally, in section 4 we discuss the chemistry of mag-

[★] Based on observations carried out with the Yebes 40m radiotelescope at Yebes Observatory, operated by the Spanish Geographic Institute (IGN, Ministerio de Transportes, Movilidad y Agenda Urbana).

nesium in IRC +10216 after the discovery of these species, and we present our conclusions in section 5.

2. Observations

The observations presented in this letter are part of very deep integrations from 31.0 to 50.3 GHz toward IRC +10216, which were carried out from May 2019 to April 2021 with the 40 meter antenna of the Centro Astronómico de Yebes (IGN, Spain) as part of the Nanocosmos project¹. The experimental setup is described in detail by Tercero et al. (2021) and further details can be found in Pardo et al. (2020). The most relevant information concerning the observations leading to the results presented in this letter are described in the remainder of this section.

The receiver consists of two HEMT cold amplifiers covering the 31.0-50.3 GHz band with horizontal and vertical polarizations. Receiver temperatures range from 22 K at 31 GHz to 42 K at 50 GHz. The backends are 16×2.5 GHz Fast Fourier Transform Spectrometers (FFTS), with a spectral resolution of 38.1 kHz, although the data were smoothed by a factor of six for their final presentation, resulting in a spectral resolution of 229 kHz.

The observations were achieved in position switching mode with an off position at 300'' in azimuth. Pointing corrections were obtained by observing the strong SiO masers of R Leo and were always within 2-3''. The intensity scale provided in the figures of this letter was antenna temperature (T_A^*) corrected for atmospheric absorption using the ATM package (Cernicharo 1985; Pardo et al. 2001). Calibration uncertainties are estimated to be within 10%. The final noise level obtained, as a function of frequency, is plotted in Figure 2.

3. Hunting new Magnesium radicals in IRC +10216

The final data product of our IRC +10216 Q-band survey consists of a 229 kHz spectrum with line fit curves and tables with the parameters of those fits and the list of molecular transitions to which they belong. The complete survey will be published shortly in a separate paper (Pardo et al. 2021). The line identification process has been done in several steps with the weakest features sometimes being confused with baseline uncertainties and needing a careful revisit of the raw data. We have used the MADEX catalog (Cernicharo 2012), the Cologne Database of Molecular Spectroscopy catalog (CDMS; Müller et al. 2005), and the JPL catalog (Pickett et al. 1998). The list of frequencies for the remaining U-lines at a given stage of the analysis was carefully checked to search for harmonic relations that could lead to finding new species.

After our publications on the identification of a series of lines belonging to MgC_3N and MgC_4H (Cernicharo et al. 2019b) and, later, on the ν_{19} mode of HC_9N (Pardo et al. 2020), other sets of spectral features, with the appearance of doublets, got our attention. All of those doublets have intensities below ~ 3 mK at the final resolution of the data set. Although they are among the weakest features arising above the noise level achieved in our survey, they can be fitted using the GILDAS Shell method to two separate components having the 14.5 km s^{-1} expansion velocity characteristic of the source. Table 1 summarizes the line parameters, whereas a selection of observed lines (and their fits) is shown in Fig. 1. Column densities and rotational temperatures were derived from rotation diagrams (see Fig. 2) using the data given in Table 1. The results are the following: $T_{\text{rot}} = 15.4 \pm 1.8$

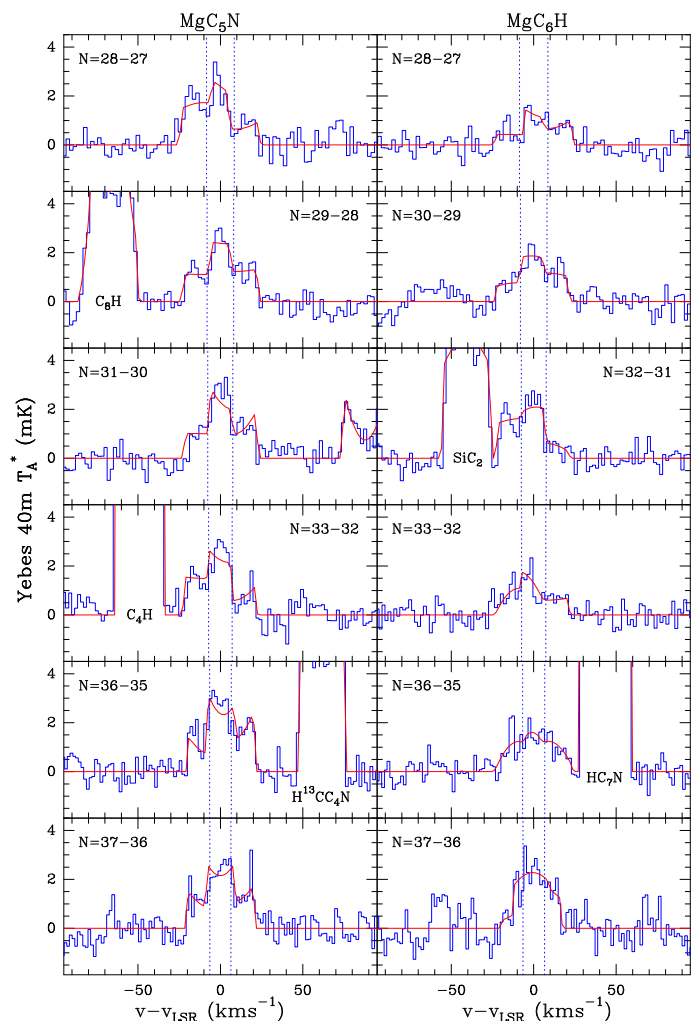


Fig. 1. Selection of the doublets corresponding to MgC_5N and MgC_6H as they appear in the IRC +10216 ultra-deep Q-band survey carried out with the Yebes 40m telescope. Data: Blue histograms. Model fit: Red curves. Calculated central frequencies of the doublets: Blue dotted lines.

K and $N_{\text{col}} = (4.7 \pm 1.3) \times 10^{12}$ for MgC_5N and $T_{\text{rot}} = 24.8 \pm 8.9$ K and $N_{\text{col}} = (2.0 \pm 0.9) \times 10^{13}$ for MgC_6H .

Even if the column density is larger for MgC_6H than for MgC_5N , as it was found for MgC_4H versus MgC_3N (Cernicharo et al. 2019b), the detection of MgC_5N is clearer because its lines are strong enough and well detected in a reliable way throughout almost the whole rotational ladder covered by our data ($N = 28-27$ to $N = 41-40$, with only $N = 42-41$ being below the noise level). The much larger dipole moment of MgC_5N (7.3 Debye) with respect to MgC_6H (2.5 Debye), as discussed later in this section, is responsible for that. In fact, the assignment to MgC_6H of the weak features shown in the right column of Fig. 1 (the most prominent in our data through its covered rotational ladder, $N = 27-26$ to $N = 42-41$) has been possible only after extra observations were scheduled and achieved in 2021. In any case, it is worth noting that for MgC_5N , we derived a lower rotational temperature than for MgC_6H , which is consistent with the higher dipole moment of the cyanide compared to the acetylide. The remainder of this section is devoted to the detailed quantum mechanical calculations carried out to do the assignments and to explore other alternatives for the carriers.

In order to obtain precise geometries and spectroscopic molecular parameters that help in the assignment of the ob-

¹ <https://nanocosmos.iff.csic.es/>

Table 1. Calculated and observational parameters of MgC₅N and MgC₆H lines in our Q-band observations of IRC +10216. Quantum numbers are N(J) for both species. Frequencies are given in MHz, energies in K, $W = \int T_{MB} dv$ in mK·kms⁻¹. We note that R is the rotational diagram = $\ln(3 k_B W/8 \pi^3 \nu_{rest} S_{ul} \mu^2)$. The symbol = in the observed frequencies means that the fitting was forced to use the calculated frequency resulting from all the other observed frequencies that could be freely fitted from the data. Blanks are left for observed parameters that could not be obtained due to blending with much stronger lines or frequencies outside the survey’s range. The boldface indicates lines shown in Figure 1.

N(J)	MgC ₅ N						MgC ₆ H					
	ν_{calc}	ν_{obs}	E_{up}	S_{ul}	W	R	ν_{calc}	ν_{obs}	E_{up}	S_{ul}	W	R
27(53/2)→26(51/2)							31305.40	31305.41	20.9	26.5	332	23.094
27(55/2)→26(53/2)							31307.36	31307.36	20.9	27.5	332	23.056
28(55/2)→27(53/2)	32278.59	32278.52	22.5	27.5	152	20.098	32464.88	32464.93	22.5	27.5	223	22.623
28(57/2)→27(55/2)	32280.40	32280.53	22.5	28.5	379	20.978	32466.84	=	22.5	28.5	74	21.489
29(57/2)→28(55/2)	33431.38	33431.36	24.1	28.5	273	20.616	33624.36	=	24.1	28.5	67	21.351
29(59/2)→28(57/2)	33433.19	33433.20	24.1	29.5	273	20.582	33626.32	33626.31	24.1	29.5	67	21.316
30(59/2)→29(57/2)	34584.17	34584.20	25.7	29.5	310	20.673	34783.84	34784.02	25.7	29.5	244	22.571
30(61/2)→29(59/2)	34585.98	34586.10	25.7	30.5	433	20.976	34785.79	34785.76	25.7	30.5	122	21.844
31(61/2)→30(59/2)	35736.95	35736.93	27.4	30.5	282	20.514	35943.31	35943.32	27.4	30.5	111	21.719
31(63/2)→30(61/2)	35738.76	35738.74	27.4	31.5	169	19.971	35945.27	35945.15	27.4	31.5	167	22.092
32(63/2)→31(61/2)	36889.72	36889.68	29.2	31.5	155	19.851	37102.79	=	29.2	31.5	102	21.567
32(65/2)→31(63/2)	36891.53	36891.22	29.2	32.5	155	19.820	37104.74	37104.61	29.2	32.5	305	22.634
33(65/2)→32(63/2)	38042.49	38042.49	31.0	32.5	143	19.705	38262.26	38262.21	31.0	32.5	94	21.422
33(67/2)→32(65/2)	38044.30	38044.36	31.0	33.5	285	20.368	38264.21	=	31.0	33.5	140	21.797
34(67/2)→33(65/2)	39195.26	39195.18	32.9	33.5	220	20.077	39421.72	=	32.9	33.5	173	21.976
34(69/2)→33(67/2)	39197.06	39197.00	32.9	34.5	307	20.384	39423.68	39423.39	32.9	34.5	346	22.640
35(69/2)→34(67/2)	40348.01	40347.94	34.9	34.5	285	20.280	40581.19		34.9	34.5		
35(71/2)→34(69/2)	40349.82	40349.69	34.9	35.5	285	20.251	40583.15	=	34.9	35.5	241	22.220
36(71/2)→35(69/2)	41500.77	41500.78	36.8	35.5	266	20.152	41740.66	41740.10	36.8	35.5	150	21.715
36(73/2)→35(71/2)	41502.57	41502.43	36.9	36.5	152	19.564	41742.61	=	36.9	36.5	112	21.400
37(73/2)→36(71/2)	42653.51	42653.55	38.9	36.5	177	19.693	42900.12	42900.43	38.9	36.5	210	21.999
37(75/2)→36(73/2)	42655.32	42655.25	38.9	37.5	177	19.666	42902.07	42901.47	38.9	37.5	70	20.873
38(75/2)→37(73/2)	43806.25	43806.45	41.0	37.5	100	19.065	44059.20		41.0	37.5		
38(77/2)→37(75/2)	43808.06	43807.98	41.0	38.5	200	19.731	44061.52	44061.53	41.0	38.5	66	20.757
39(77/2)→38(75/2)	44958.98	44958.88	43.2	38.5	94	18.952	45219.04		43.2	38.5		
39(79/2)→38(77/2)	44960.79	44960.46	43.2	39.5	157	19.437	45220.99		43.2	39.5		
40(79/2)→39(77/2)	46111.71	46111.60	45.4	39.5	118	19.132	46378.49	=	45.4	39.5	146	21.480
40(81/2)→39(79/2)	46113.51	46113.74	45.4	40.5	178	19.512	46380.45		45.4	40.5		
41(81/2)→40(79/2)	47264.42	47264.57	47.6	40.5	168	19.434	47537.94		47.6	40.5		
41(83/2)→40(81/2)	47266.23	47266.21	47.6	41.5	84	18.716	47539.90		47.6	41.5		
42(83/2)→41(81/2)	48417.14		50.0	41.5			48697.40	48697.07	50.0	41.5	158	21.460
42(85/2)→41(83/2)	48418.94		50.0	42.5			48699.35		50.0	42.5		

served lines, we carried out high-level ab initio calculations for the following two possible candidates: MgC₅N and MgC₆H. All the calculations were performed using the Molpro 2020.2 (Werner et al. 2020) and Gaussian09 (Frisch et al. 2013) program packages. The geometry optimization calculations were carried out at the CCSD(T)-F12/cc-pCVTZ-F12 level of theory (Raghavachari et al. 1989; Adler et al. 2007; Knizia et al. 2009; Hill et al. 2010a,b), which has been proved as a suitable method to accurately reproduce the molecular geometry of analog molecules (Cernicharo et al. 2019b). We followed the same strategy previously used by us for the related molecular systems MgC₃N and MgC₄H (Cernicharo et al. 2019b). In this manner, we scaled our calculations for MgC₅N and MgC₆H using the experimental and theoretical results of MgC₃N and MgC₄H, respectively.

According to our calculations, the electronic ground state for MgC₅N and MgC₆H is ²Σ. The calculated spectroscopic parameters for both species are shown in Table 2, together with those for MgC₃N and MgC₄H. As expected, the *B*, *D_N*, and γ values for MgC₅N and MgC₆H are quite similar. However, large differences were found between the predicted dipole moments, being 7.3 D and 2.5 D for MgC₅N and MgC₆H, respectively. A

comparison of the scaled values with those obtained from fitting the IRC +10216 lines allowed us to assign the two series of lines to MgC₅N and MgC₆H. The relative errors for the *B* constant are 0.024% and 0.017% for MgC₅N and MgC₆H, respectively. For γ values, the errors are larger, 2.8% and 4.1% for MgC₅N and MgC₆H, respectively. Similar discrepancies were found for MgC₃N and MgC₄H (see Table 2). For *D_N*, the agreement between calculated and determined values for MgC₅N is very good, within around 4%. However, for MgC₆H, the *D_N* value was not determined from our fit and, thus, a comparison with the ab initio values makes no sense.

As the doublets of MgC₅N are directly unquestionable from the data, those of MgC₆H, due to a lower signal-to-noise ratio, require further support in particular to rule out ¹Σ species. In fact, there are not many alternatives to MgC₆H, basically the C₇N radical and the C₇N⁻ anion as their theoretical rotational constants *B* are 583.1 and 582.0 MHz, respectively (Botschwina et al. 1997; Botschwina & Oswald 2008).

The anion C₇N⁻ is predicted to have a ¹Σ electronic ground state (Botschwina & Oswald 2008) and thus it could be an alternative to MgC₆H. However, even if a lower noise level should be desirable, the observed line widths are too large for a ¹Σ species.

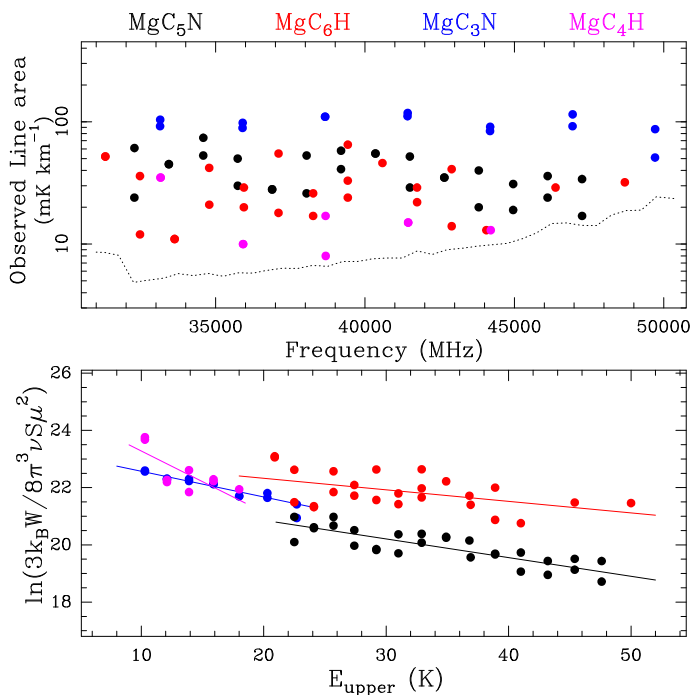


Fig. 2. Observed integrated line areas of MgC_3N , MgC_4H , MgC_5N , and MgC_6H toward IRC+10216 in the Q-band, and the rotational diagram for each molecule built from those integrated areas, together with the best fits that provide an estimation of their column densities and rotational temperatures. The dotted curve in the top panel is the noise level achieved in our survey across the whole frequency range. A few lines beyond 44 GHz are below the detectability limit and for this reason they do not appear in Table 1.

Moreover, the C_7N radical itself should be present in our data, but we have no evidence of lines related by half integer quantum numbers that could be assigned to it as its electronic ground state was calculated to be $^2\Pi$ (Botschwina et al. 1997).

4. Magnesium chemistry in IRC +10216

The formation of MgC_5N and MgC_6H in IRC +10216 occurs very likely through the same mechanism that forms other smaller magnesium cyanides and acetylides previously detected in this same source, that is, MgNC , MgCN , HMgNC , MgC_3N , MgCCH , and MgC_4H . Based on the work of Petrie (1996), the synthesis of these types of molecules is thought to proceed through a two-step gas-phase mechanism in which large cyanopolynes and polyynes associate radiatively with Mg^+ and then the $\text{Mg}^+/\text{NC}_{2n+1}\text{H}$ and $\text{Mg}^+/\text{C}_{2n}\text{H}_2$ complexes fragment upon dissociative recombination with electrons (Millar 2008; Cabezas et al. 2013; Cernicharo et al. 2019b).

Here we have expanded the chemical network used in Cernicharo et al. (2019b) to include the larger species MgC_5N and MgC_6H . The chemical model of the outer envelope is based on Agúndez et al. (2017). As in Cernicharo et al. (2019b), the rate coefficients for the radiative associations of Mg^+ with polyynes and cyanopolynes are taken from Dunbar & Petrie (2002) and we assume that open shell metal-containing species (MgNC , MgCN , MgC_3N , MgC_5N , MgCCH , MgC_4H , and MgC_6H) react with electrons and H atoms, while closed shell molecules (HMgNC being the only one considered) do not react. The ion complexes $\text{Mg}^+/\text{NC}_{2n+1}\text{H}$ and $\text{Mg}^+/\text{C}_{2n}\text{H}_2$ may have multiple channels of fragmentation when reacting with electrons. The branching ratios of each channel are unknown,

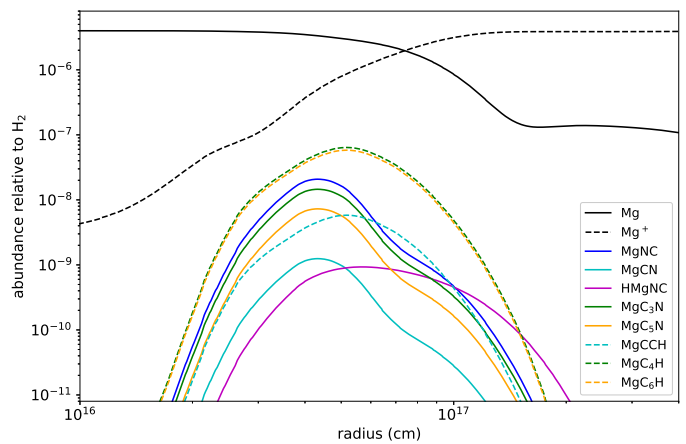


Fig. 3. Abundances calculated with the chemical model for Mg , Mg^+ , and all Mg-bearing molecules detected in IRC +10216.

although they are key since they are the main parameters that set the relative abundances between the different magnesium cyanide derivatives and between the various magnesium acetylides. As in Cernicharo et al. (2019b), we adjusted these branching ratios to reproduce the relative abundances observed.

First of all, if we look at the magnesium cyanides, we find that their observed relative abundances follow this sequence: $\text{MgNC}/\text{HMgNC}/\text{MgCN}/\text{MgC}_3\text{N}/\text{MgC}_5\text{N} \sim 1/0.05/0.06/0.7/0.35$ (Cabezas et al. 2013; Cernicharo et al. 2019b; this work). We find that to reproduce these ratios, the branching ratios of the channels yielding MgCN , HMgNC , MgC_3N , and MgC_5N must be 0.05, 0.01, 0.7, and 0.35 of that yielding MgNC . These values, which are similar to those given in Cernicharo et al. (2019b), roughly correspond to the column density ratios observed, except for HMgNC , which in the chemical model is assumed to have a slower destruction rate due to its closed shell nature.

For the magnesium acetylides, the observed column density ratios are $\text{MgCCH}/\text{MgC}_4\text{H}/\text{MgC}_6\text{H} \sim 1/11/10$ and we find that the branching ratios of the channels yielding MgC_4H and MgC_6H must be 11 and 10 times of that yielding MgCCH , which precisely follow the observed relative abundances since the three acetylides are open shell species and thus are assumed to have similar destruction rates. Mauron & Huggins (2010) did not observe atomic Mg in the outer layers of IRC +10216 and thus the abundance of atomic Mg is not well constrained. Here we adopted an initial abundance of Mg relative to H of 2×10^{-6} , which accounts for about 5% of the cosmic abundance of Mg and allowed us to reproduce the absolute column densities of the magnesium cyanides and acetylides observed. For example, the calculated column density of MgC_5N is $2.8 \times 10^{12} \text{ cm}^{-2}$, while for MgC_6H we calculated $2.6 \times 10^{13} \text{ cm}^{-2}$, which are only slightly below and above the values derived from the observations, respectively. The results from the chemical model are shown in Fig. 3.

It is interesting to note that MgNC should be significantly favored in the dissociative recombination of $\text{Mg}^+/\text{NC}_{2n+1}\text{H}$ complexes, compared to the larger magnesium cyanides MgC_3N and MgC_5N . However, in the case of $\text{Mg}^+/\text{C}_{2n}\text{H}_2$ complexes, the larger acetylides MgC_4H and MgC_6H should be strongly favored compared to MgCCH . It would be interesting to verify this point, which directly arises from the observed relative abundances in IRC +10216, by studying the dissociative recombination of these complexes. If large fragments tend to be favored, it would not be

Table 2. Spectroscopic parameters B , D_N , and γ for MgC₃N, MgC₅N, MgC₄H, and MgC₆H (all in MHz).

Parameter	MgC ₃ N		MgC ₅ N		
	Calc. ^a	Exp. ^b	Calc. ^a	Scaled ^c	Exp. ^d
B	1376.50	1380.888	574.74	576.57	576.43106(125)
D_N	0.0640×10^{-3}	0.0760×10^{-3}	5.87×10^{-6}	6.98×10^{-6}	$7.325(483) \times 10^{-6}$
γ	4.09	4.35	1.64	1.75	1.8071(386)

Parameter	MgC ₄ H		MgC ₆ H		
	Calc. ^a	Exp. ^b	Calc. ^a	Scaled ^c	Exp. ^d
B	1377.38	1381.512	578.11	579.85	579.75150(459)
D_N	0.0601×10^{-3}	0.074×10^{-3}	5.83×10^{-6}	7.02×10^{-6}	$2.53(214) \times 10^{-6}$
γ	4.43	4.7	1.76	1.87	1.9551(141)

Notes.

^(a) This work. The B rotational constant was calculated at the CCSD(T)-F12/cc-pCVTZ-F12 level of theory, while D_N and γ constants were calculated at the MP2/cc-pVTZ level of theory.

^(b) Cernicharo et al. (2019b).

^(c) This work; scaled by the ratio Exp/Calc. of the corresponding parameter for MgC₃N and MgC₄H species, see text .

^(d) This work.

surprising that even larger members of the series of magnesium cyanides and acetylides such as MgC₇N and MgC₈H could be present in IRC +10216 with abundances comparable to those of MgC₅N and MgC₆H, respectively.

5. Conclusions

This work has extended the catalog of molecular species found for the first time in IRC+10216, and in space, with the following two new members: MgC₅N and MgC₆H. But, more interestingly, their column densities have been found to be not so different from their shorter counterparts so that it could be possible to find longer magnesium cyanides and acetylides in IRC +10216. This and other recent results from our group suggest that new receivers covering the ~23-31 GHz range should be a major priority for the Yebes 40m radiotelescope, as they could lead to new and interesting findings of heavy molecules in objects such as IRC+10216 or TMC-1 that would have an important impact on our understanding of astrochemistry.

A forthcoming paper will present the results of the whole Yebes IRC+10216 Q-band survey. In it, the number of U-lines has been drastically reduced due to the progress made in line catalogs thanks to works as this one, with two molecular species being spectroscopically characterized from astronomical data without any previous laboratory data.

Acknowledgements. We thank Ministerio de Ciencia e Innovación of Spain (MICIU) for funding support through projects AYA2016-75066-C2-1-P, PID2019-106110GB-I00, PID2019-107115GB-C21 / AEI / 10.13039/501100011033, and PID2019-106235GB-I00. We also thank ERC for funding through grant ERC-2013-Syg-610256-NANOCOSMOS. M.A. thanks MICIU for grant RyC-2014-16277.

References

Adler, T. B., Knizia, G., Werner, H.-J., 2007 J. Chem. Phys. 127, 221106
 Agúndez, M., Cernicharo, J., & Guélin, M. 2014, A&A, 570, A45
 Agúndez, M., Cernicharo, J., Quintana-Lacaci, G., et al., 2017, A&A, 601, A4
 Botschwina, P., Horn, M., Markey, K., & Oswald, R., 1997, Mol.Phys., 92, 381

Botschwina, P. & Oswald, R., 2008, J. Chem. Phys. 129, 044305
 Cabezas, C., Cernicharo, J., Alonso, J. L., et al., 2013, ApJ, 775, 133
 Cernicharo, J., 1985, Internal IRAM report (Granada: IRAM)
 Cernicharo, J. & Guélin, M., 1987, A&A, 183, L10
 Cernicharo, J., 2012, in ECLA 2011: Proc. of the European Conference on Laboratory Astrophysics, EAS Publications Series, 2012, Ed.: C. Stehl, C. Joblin, & L. d'Hendecourt (Cambridge: Cambridge Univ. Press), 251; https://nanocosmos.iff.csic.es/?page_id=1619
 Cernicharo, J., Velilla-Prieto, L., Agúndez, M., et al., 2019a, A&A, 627, L4
 Cernicharo, J., Cabezas, C., Pardo, J. R., et al., 2019b, A&A, 630, L2
 Cernicharo, J., Agúndez, M., Cabezas, C., et al., 2021, A&A, 649, L15
 Dunbar, R. C. & Petrie, S. 2002, ApJ, 564, 792
 Frisch, M. J., Trucks, G. W., Schlegel, H. B., et al. 2013, Gaussian 09, rev. D.01
 Guélin, M., Lucas, R., & Cernicharo, J., 1993, A&A, 280, L19
 Guélin, M., Müller, S., & Cernicharo, J., 2000, A&A, 363, L9
 Guélin, M., Müller, S. Cernicharo, J., et al., 2004, A&A, 426, L49
 Kawaguchi, K., Kagi, E., Hirano, T., et al., 1993, ApJ, 406, L39
 Knizia, G., Adler, T. B., Werner, H.-J., 2009, J. Chem. Phys. 130, 054104
 Hill, J. G., Mazumder, S., Peterson, K. A., 2010a, J. Chem. Phys., 132, 054108
 Hill, J. G. & Peterson, K. A., 2010b, Phys. Chem. Chem. Phys., 12, 10460
 Mauron, N. & Huggins, P. J., 2010, A&A, 513, A31
 Millar, T. J. 2008, Ap&SS, 313, 223
 Müller, H.S.P., Schlöder, F., Stutzki, J., Winnewisser, G. 2005, J. Mol. Struct., 742, 215
 Pardo, J. R., Cernicharo, J., Serabyn, E. 2001, IEEE Trans. Antennas and Propagation, 49, 12
 Pardo, J. R., Bermúdez, C., Cabezas, C., et al., 2020 A&A, 640, L13
 Pardo, J. R., Cernicharo, J., Tercero, B., et al., 2021 A&A, in prep.
 Petrie, S. 1996, MNRAS, 282, 807
 Pickett, H.M., Poynter, R. L., Cohen, E. A., et al. 1998, J. Quant. Spectrosc. Radiat. Transfer, 60, 883
 Pulliam, R. L., Savage, C., Agúndez, M., et al., 2010, ApJ, 725, L181
 Raghavachari, K., Trucks, G. W., Pople, J. A., Head-Gordon, M., 1989, Chem. Phys. Lett., 157, 479
 Tercero, F., López-Pérez, J. A., Gallego, J. D., et al., 2021, A&A, 645, A37
 Turner, B. E., Steimle, T. C., & Meerts, L., 1994, ApJ, 426, L97
 Werner, H.-J., Knowles, P. J., Knizia, G., et al., 2020, MOLPRO, version 2020.2
 Zack, L. N., Halfen, D. T. & Ziurys, L. M., 2011, ApJ, 733, L36
 Ziurys, L. M., Apponi, A. J., Guélin, M., & Cernicharo, J., 1995, ApJ, 445, L47
 Ziurys, L. M., Savage, C., Highberger, J. L., et al., 2002, ApJ, 564, L45